Electrochimica Acta 255 (2017) 463–471

Contents lists available at ScienceDirect

Electrochimica Acta

journal homepage: www.elsevier.com/locate/electacta

pH fronts and tissue natural buffer interaction in gene electrotransfer protocols

M. Marino[a,b,d], N. Olaiz[a,b,d], E. Signori[c], F. Maglietti[a,b,d], C. Suárez[a,b,d], S. Michinski[a,b,d], G. Marshall[a,b,d,*]

[a] Laboratorio de Sistemas Complejos, Departamento de Computación,Facultad de Ciencias Exactas y Naturales, Universidad de Buenos Aires, Argentina
[b] Instituto de Física del Plasma, Departamento de Física, Facultad de Ciencias Exactas y Naturales, Universidad de Buenos Aires, Argentina
[c] Laboratory of Molecular Pathology and Experimental Oncology, CNR-IFT, Rome, Italy
[d] Consejo Nacional de Investigaciones Científicas y Técnicas, Argentina

ARTICLE INFO

Article history:
Received 17 February 2017
Received in revised form 25 August 2017
Accepted 4 September 2017
Available online 7 September 2017

Keywords:
Gene electrotransfer
Electrochemotherapy
electrolytic ablation
irreversible electroporation
pH front tracking

ABSTRACT

Gene electrotransfer (GET) protocols, based on the introduction into the cells of genes encoding immunomodulatory molecules, constitute a safe and powerful strategy for inducing an immune response against cancer. But GET efficiency can be significantly affected by damage due to the products of electrolysis, in particular, pH fronts. To elucidate the role of pH fronts and damage in GET efficiency we present an analysis of the pH fronts-tissue natural buffer interaction through a theoretical model using the Nernst-Planck equations for ion transport assuming a tissue with a bicarbonate buffering system and its validation with experimental measurements. pH front-buffer interaction measurements unveil a remarkable behavior tuned by pulse length and frequency: during the ON pulse critical pH front trajectories (pH=8.5 or 5.5) jump forward, during the OFF pulse, they recede due to tissue natural buffer attenuation. Theory shows that they are intimately related to ion transport mode: during the ON pulse, ion transport is mainly governed by migration and trajectories jump forward in time; during the OFF pulse, migration ceases, ion transport is governed solely by diffusion and trajectories recede due to buffer attenuation. Experiments and theory show that regardless of the presence of buffer attenuation, pH fronts remain during several minutes in a non-physiological state after the treatment. These results suggest that regions enclosed by pH fronts trajectories (thus subjected to non-physiological pH values during a sufficiently long time) may be subjected to plasmid damage during a GET treatment. Ways to minimize this effect, thus optimizing GET efficiency are suggested.

1. Introduction

Electroporation or electropermeabilization is a phenomenon in which cell membrane permeability is augmented through the application of pulsed electric fields, thus increasing cell membrane mass transfer mechanisms. Many applications of electroporation appeared in the last decade in different areas such as in medicine, biotechnology, food processing and environmental preservation [1]. In medicine, some of the foremost tumor treatments based on electroporation, ie.: electrochemotherapy (ECT), irreversible electroporation (IRE) and gene electrotransfer (GET), are being used with exceptional results. ECT combines the administration of a low dose of a chemotherapeutic agent (such as bleomycin or cisplatin), non-permeant to the cell membrane, with reversible electroporation, thus potentiating its entry into the cell [2–4]. IRE is an ablative technique not requiring drugs and possessing the advantage over other ablative techniques, of preserving extracellular matrix, vessels and nerves [5,6]. GET, consisting of the combination of electroporation and the injection of a gene (usually DNA), is a very efficient non-viral gene delivery technique that is being used in many diseases [7,9,10,8]. Although the mechanisms of GET have not been completely elucidated [11], it is supposed that a higher DNA uptake in vivo is achieved not only due to increased cell membrane permeability but to the migration effect of the electric field [12]. Another non-thermal tumor ablative treatment that uses very long electric pulses of very low intensity is Electrolytic Ablation (EA), also called electrochemical treatment of tumors (EChT). It consists of the application of an electric current through two or more electrodes inserted in the tissue thus generating electrolytic products that induce tumor necrosis (see details in

* Corresponding author. Tel.: +54 11 4576 3390 ext.709; fax: +54 11 4576 3359.
E-mail address: marshalg@retina.ar (G. Marshall).

http://dx.doi.org/10.1016/j.electacta.2017.09.021
0013-4686/

[13]). Recently, EA combined with reversible EP was shown to augment the extent of tissue ablation in comparison to that obtained with EA alone [14].

Physiological processes, such as respiration, blood circulation, and renal excretion, regulate the dynamic stability of the internal medium and therefore of the cell. This phenomenon is known as homeostasis. In particular, acid-base homeostasis exerts a major influence on protein function, thereby critically affecting tissue and organ performance. The internal pH of most living cells is close to 7.4. To maintain the stability of organs and tissues, buffering system is of crucial importance. Though bicarbonate, proteins and organic phosphate are the principal buffer systems in tissue, bicarbonate buffer system prevails in plasma and interstitial fluid; for this reason, it was selected for our study. In bicarbonate buffer, carbon dioxide (CO_2) reacts with water (H_2O) to form carbonic acid (H_2CO_3) that rapidly dissociates to form a bicarbonate ion (HCO_3^-) and a hydrogen ion (H^+) i.e.

$$CO_2 + H_2O \rightleftharpoons H_2CO_3$$

$$H_2CO_3 \rightleftharpoons HCO_3^- + H^+$$

When an excessive amount of H^+ in a tissue is revealed, the buffering system releases HCO_3^- forming carbonic acid, reducing the amount of H^+ in the medium. When there is an excessive amount of OH^- in a tissue, this is combined with CO_2 to form HCO_3^- and with HCO_3^- to form H_2O and CO_3^{2-}, thus neutralizing pH alterations:

$$OH^- + CO_2 \rightleftharpoons HCO_3^-$$

$$OH^- + HCO_3^- \rightleftharpoons CO_3^{2-} + H_2O$$

The presence of strong pH fronts due to the electrolysis process during the application of GET protocols is a well-known fact. These pH fronts may produce plasmid and cell damage. Plasmid damage occurs because DNA is seriously affected by pH. Plasmid denaturation occurs when exposed to an alkaline medium above 8.4 or an acid medium below 4.5. In fact, at pH = 12.5 [4,15,16] plasmids are permanently denatured in less than 1 second. On the other hand, cell death occurs when exposed to an alkaline medium above 9 or an acid medium below 5.5 [17]. In [18] it was shown that, in spite of the presence of natural buffers, significant pH changes occur in tissues when GET pulses are applied. For instance, it is shown that immediately after the application of a GET protocol (using superficial electrodes in an ex vivo model), pH changes lasted a couple of minutes. In [19] it was shown through theory and experimental measurements in an in vivo dorsal skinfold chamber GET model protocol, the existence of pH fronts emerging from both electrodes and that these fronts are immediate and substantial, thus giving rise to damage. It was also shown that after the last pulse applied, pH neutralization lasted several minutes.

The theoretical results previously discussed regarding the extent of tissue damage due to pH fronts [19] were obtained through a model in which tissue was treated as an aqueous solution of sodium chloride; though this and previous theoretical models advanced our knowledge of electrolytic effects in tissue damage, the presence of tissue natural buffering was not specifically taken into consideration. This raises the question of the extent in which tissue natural buffer would attenuate or eliminate damage due to pH fronts.

Natural buffering modeling was firstly treated in a series of papers of electrolytic ablation (EA) protocols [20–22]. In the first EA model the tissue was treated as an aqueous solution of sodium chloride; in the second model, a bicarbonate buffer system was taken into account, and in the third model the transport of chlorine and chlorinated species was added. The open question of whether natural buffer attenuation would significantly diminish GET damage due to pH fronts was theoretically elucidated in [8]. In that work, an in silico modeling of GET damage considering the presence of tissue natural buffering was presented. The model is based on previous works of the authors in EA and EP and in the works of [20–22] in EA.

The aim of this work was to deepen our understanding of the role of pH fronts in damage, thus in GET efficiency. This is done through an analysis of pH fronts-natural buffer interaction using the Nernst-Planck equations for ion transport, assuming a tissue with a bicarbonate buffering system and validating it with experimental measurements. Analysis of pH fronts-natural buffer interaction may suggest ways to minimize GET damage, thus optimize GET efficiency.

2. Materials and Methods

2.1. In vivo *modeling*

pH measuring was done extending measurements of an in vivo model introduced in [19]. The model consisted of a transparent chamber implanted in the dorsal skinfold of a female mouse (6- to 8-weeks-old BALB-c/J) under general anesthesia. Intravital microscopy was done with an Olympus BX41 fluorescent microscope. Experiments consisted of the application of electric pulses using 27-gauge needles electrodes with a 2 mm separation, inserted through the skin (thickness 0.6 mm). Two different protocols were used: protocol one, consisted of 10 pulses with a duration of 20 ms each at 1Hz and voltages of 20, 40 and 60 V; protocol 2, consisted of 10 pulses with a duration of 10 ms each, at 10Hz and voltages of 20, 40 and 60 V. Fig. 1 (top) depicts a sketch of the experimental setup showing the camera, mirror, objectives, a mouse with a dorsal skinfold chamber and the BTX ECM 830 (Harvard Apparatus, USA)

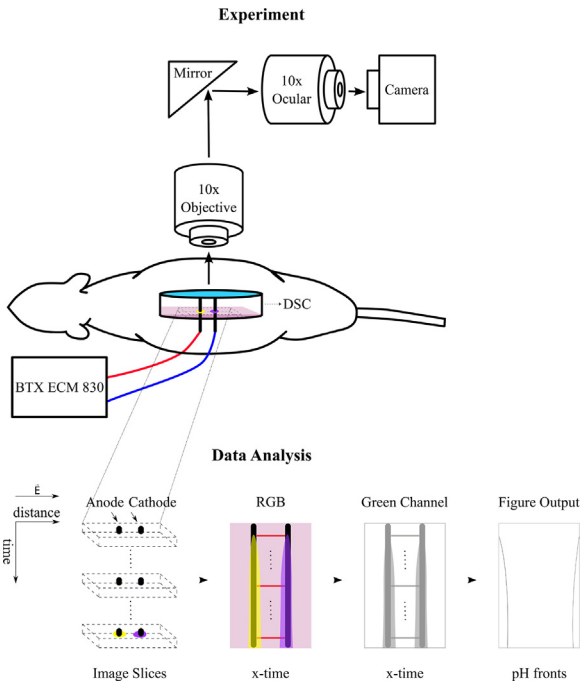

Fig. 1. Sketch of the experimental setup showing the camera, mirror, objectives, a mouse with a dorsal skinfold chamber (DSC) and the BTX ECM 830 square wave generator (top). The space-time coordinates chosen, the electric field orientation and the steps for image acquisition: piling up of frames in time, with image slices; x-time RGB; x-time green channel; and pH front trajectories (bottom).

square wave generator. Fig. 1 (bottom) presents the space-time coordinates chosen, the electric field orientation and the steps for image acquisition (later discussed).

pH fronts advance was recorded with a Casio ex-fh25 camera (30 fps, 33 ms opening, and 1280 x 720 resolution). pH visualization was done through phenol red ($C_{19}H_{14}O_5S$) as acid as well as basic pH indicators (6.8-8.2, yellow to red, SIGMA). The pH indicator was superficially applied before the beginning of the recording. Upon application of the electric pulses, the pH indicator underwent a visible color change which is recorded by the camera. Images (RGB format, 100x magnification, 1280 x 720 pixels at a 16-bit depth) were analyzed with the ImageJ software (ImageJ, http://rsbweb.nih.gov/ij). Since the pH indicator is better depicted in the green channel, thus producing a more accurate segmentation, it was chosen as the only component for the pH color analysis. The time evolution of the pH front-buffer interaction during the electroporation process is revealed by a space-time diagram constructed following the steps sketched in Fig. 1 (bottom). In this figure, the space-time coordinates chosen, the electric field orientation and the steps (in lexicographic ordering) for image acquisition, are presented: the first sketch shows the piling up of frames (images) in time, each one with its image slice; the second, the resulting x-time RGB; the third, the resulting x-time green channel; and the last sketch, the resulting pH front trajectories. Following the previous steps, to compute the pH trajectory, in each frame (image), a line (slice) was plotted between the two electrode centers (the x-direction) and the color variation of the pH indicator over this line was recorded. Then, these lines were stacked to yield the space-time (x-time image) spanning the duration of the experiment. In each line, the distance to the anode or cathode in which an abrupt color change took place was determined using the ImageJ edge detection tool; this distance defined the pH front position at a given time. With the resulting stack of pH front positions in time, pH trajectories were reconstructed. Measurements were calibrated with a graticule (Graticules Ltd. Tonbridge, Kent). Animals were maintained in accordance with current regulations and standards of the NIH. Experimental protocols were designed according to the regulations of the committee for the care and use of laboratory animals of our institution (CICUAL)

2.2. In silico *modeling*

In silico modeling is aimed at predicting the role of pH in damage, in the application of a GET protocol to the DSC experimental results previously described. pH variation is obtained through the solution of the Nernst-Planck equations describing the electric field and ion transport in a seven-component species solution (H^+, OH^-, Cl^-, Na^+, HCO_3^-, CO_2 and CO_3^{2-}). Although the electric field distribution is a 3D phenomenon (parallel-needle electrodes), in order to simulate Nernst-Planck equation describing ion transport between the two needle electrodes, a 1D approximation was used in which the electric field varies over the anode-cathode distance (the line joining the two electrode centers, see Fig. 1 bottom).

Following [23] and [24], material balance for specie $B \in \{H^+, OH^-, Cl^-, HCO_3^-, CO_2, CO_3^{2-}\}$ is given by:

$$\frac{\partial C_B}{\partial t} + \nabla \cdot \boldsymbol{N_B} = R_B \tag{1}$$

where he molar flux $\boldsymbol{N_B}$ is:

$$\boldsymbol{N_B} = -D_B \nabla C_B - \frac{z_B}{|z_B|} u_B C_B \nabla \Phi \tag{2}$$

where C_B and Φ are the concentration and electric potential, respectively. D_B, z_B and u_B are the diffusion coefficient, charge number (with sign) and mobility of the species B, respectively, and t is the time. R_B represents the production of species B through the following chemical reactions in the electrolyte:

$$H^+ + OH^- \underset{k_{3,b}}{\overset{k_{3,f}}{\rightleftharpoons}} H_2O \tag{3}$$

$$H^+ + HCO_3^- \underset{k_{4,b}}{\overset{k_{4,f}}{\rightleftharpoons}} CO_2 + H_2O \tag{4}$$

$$OH^- + CO_2 \underset{k_{5,b}}{\overset{k_{5,f}}{\rightleftharpoons}} HCO_3^- \tag{5}$$

$$OH^- + HCO_3^- \underset{k_{6,b}}{\overset{k_{6,f}}{\rightleftharpoons}} CO_3^{2-} + H_2O \tag{6}$$

where $k_{j,f}$ and $k_{j,b}$ are the forward and backward rate constants of the homogeneous reaction j, respectively. The reaction terms in

Table 1
In silico model parameters.

Parameter	Value	Ref	Parameter	Value	Ref
D_{H^+}	$12.5 \cdot 10^{-9}\ m^2\ s^{-1}$	[25]	D_{OH^-}	$7.05 \cdot 10^{-9}\ m^2\ s^{-1}$	[25]
D_{Na^+}	$1.78 \cdot 10^{-9}\ m^2\ s^{-1}$	[25]	D_{Cl^-}	$2.72 \cdot 10^{-9}\ m^2\ s^{-1}$	[25]
$D_{HCO_3^-}$	$1.49 \cdot 10^{-9}\ m^2\ s^{-1}$	[25]	$D_{CO_3^{2-}}$	$2.46 \cdot 10^{-9}\ m^2\ s^{-1}$	[34]
D_{CO_2}	$2.71 \cdot 10^{-9}\ m^2\ s^{-1}$	[35]			
$C^0_{H^+}$	$10^{-4.4}\ mol\ m^{-3}$	[36]	$C^0_{OH^-}$	$10^{-3.2}\ mol\ m^{-3}$	[36]
$C^0_{Na^+}$	$160\ mol\ m^{-3}$	[36]	$C^0_{Cl^-}$	$132.912\ mol\ m^{-3}$	[36]
$C^0_{HCO_3^-}$	$27\ mol\ m^{-3}$	[36]	$C^0_{CO_3^{2-}}$	$4.4 \cdot 10^{-2}\ mol\ m^{-3}$	[22]
$C^0_{CO_2}$	$1.3\ mol\ m^{-3}$	[22]	$C^0_{H_2O}$	$55500\ mol\ m^{-3}$	
$k_{3,f}$	$1.5 \cdot 10^8\ m^3\ mol^{-1}\ s^{-1}$	[37]	$k_{3,b}$	$6.79 \cdot 10^{-5}\ s^{-1}$	[21]
$k_{4,f}$	$310\ m^3\ mol^{-1}\ s^{-1}$	[37]	$k_{4,b}$	$4.62 \cdot 10^{-6}\ s^{-1}$	[21]
$k_{5,f}$	$20\ m^3\ mol^{-1}\ s^{-1}$	[22]	$k_{5,b}$	$6.08 \cdot 10^{-4}\ s^{-1}$	[22]
$k_{6,f}$	$1.5 \cdot 10^8\ m^3\ mol^{-1}\ s^{-1}$	[22]	$k_{6,b}$	$58076755.57\ s^{-1}$	[22]
T	$310\ K$		R	$8.31\ kg\ m^2\ K^{-1}\ mol^{-1}\ s^{-2}$	
F	$96485.3415\ A\ s\ mol^{-1}$				

tissue are:

$$\begin{aligned}
R_{H^+} &= k_{3,b}\,C_{H_20} + k_{4,b}\,C_{CO_2}\,C_{H_20} - k_{3,f}\,C_{H^+}\,C_{OH^-} - k_{4,f}\,C_{H^+}\,C_{HCO_3^-}\\
R_{OH^-} &= -k_{5,f}\,C_{CO_2}\,C_{OH^-} + k_{5,b}\,C_{HCO_3^-} - k_{6,f}\,C_{HCO_3^-}\,C_{OH^-} + k_{6,b}\,C_{CO_3^{2-}}\\
&\quad + k_{3,b}\,C_{H_20} - k_{3,f}\,C_{H^+}\,C_{OH^-}\\
R_{HCO_3^-} &= k_{4,b}\,C_{CO_2}\,C_{H_20} - k_{4,f}\,C_{H^+}\,C_{HCO_3^-} + k_{5,f}\,C_{CO_2}\,C_{OH^-} - k_{5,b}\,C_{HCO_3^-}\\
&\quad - k_{6,f}\,C_{HCO_3^-}\,C_{OH^-} + k_{6,b}\,C_{CO_3^{2-}}\\
R_{CO_2} &= -k_{5,f}\,C_{CO_2}\,C_{OH^-} + k_{5,b}\,C_{HCO_3^-} + k_{4,f}\,C_{H^+}\,C_{HCO_3^-} - k_{4,b}\,C_{CO_2}\,C_{H_20}\\
R_{CO_3^{2-}} &= k_{6,f}\,C_{HCO_3^-}\,C_{OH^-} - k_{6,b}\,C_{CO_3^{2-}}\\
R_{Cl^-} &= R_{Na^+} = 0
\end{aligned}$$

Values of backward and forward rate constants are presented in Table 1 and explained in detail in [21,22].

The concentration of the seventh specie (Na^+) is obtained via the electroneutrality condition:

$$\sum_B z_B\,C_B = 0 \tag{7}$$

The electrostatic potential Φ can be calculated from the charge conservation condition

$$\nabla \cdot \boldsymbol{j_T} = 0 \tag{8}$$

where the total current density $\boldsymbol{j_T}$ is given by

$$\boldsymbol{j_T} = F\sum_B z_B\,\boldsymbol{N_B} \tag{9}$$

Taking into account expression for molar flux (2) and Faraday's law, equation (8) can be rewritten as:

$$\sum_B z_B D_B \nabla^2 C_B + \sum_B |z_B| u_B \nabla\cdot(C_B \nabla\Phi) = 0 \tag{10}$$

The electric field is obtained via

$$\boldsymbol{E} = -\nabla\Phi \tag{11}$$

The ionic mobility and diffusion coefficient are related through the Nernst-Einstein equation:

$$D_B = \frac{RT}{|z_B|F}u_B \tag{12}$$

where T is the absolute temperature, R the universal gas constant and F the Faraday's constant.

Diffusion coefficients in water [25] were adapted to describe diffusion in a tissue medium as follows:

$$D_B = d\,D_B^{Water} \tag{13}$$

where D_B is an effective diffusion coefficient coming from the assumption of a tissue seen as a porous medium [26], D_B^{Water} is the diffusion coefficient in water and d (fitted from experiments) is a factor that reduces the diffusion coefficient in a porous medium relative to the diffusion coefficient in water and takes the value of 0.2.

Following Nilsson [22], the initial bicarbonate concentration for the bicarbonate buffer system is 27 mM. The initial hydroxyl concentration is calculated using pK_w = 13.6 [27]. The initial sodium concentration is 0.16 M and pH = 7.4. These concentrations are closed to those found in plasma and interstitial fluid [28]. Carbon dioxide (CO_2) and carbonate (CO_3^{2-}) concentrations come from the equilibrium reactions (5) and (6), respectively. The electroneutrality condition is used to calculate the initial chloride (Cl^-) concentration.

Equations (1), (7), (10), (11) plus boundary conditions (explained in detail in [24]) are used to solve the concentrations and potential fields in a space domain defined by the geometry in Fig. 1 and time.

Following [23], the Nernst-Planck system of partial differential equations is split in time in a two-step procedure. During the first time step with the ON pulse, electric current circulates and transport is governed mainly by migration and diffusion; during the second time step with the OFF pulse, electric current circulation ceases and transport is governed solely by diffusion. This results in a multi-time step model in which the first time step is several orders of magnitude smaller than the second time step (to account for the migration in the microsecond scale). The split system is solved, successively in time, in a fixed domain on a one-dimensional space and time uniform grid using strongly implicit finite differences (details can be found in [29]). The nonlinear equation resulting from the approximation of the boundary conditions is solved by Newton's method (details can be found in [30]). The simulation starts in the first time step with the pulse in ON. At t=0, there are no concentration gradients throughout the electrolyte. Input parameters for the computational model are taken from Table 1. During the second time step with the pulse in OFF, the system is solved using as initial conditions the solution obtained from the first step.

3. Results and Discussion

In this section we first present in Fig. 2 an image showing the existence of pH fronts through an in vivo model. Then we present in Figs. 3 and 4 the influence of including tissue buffer effects through a comparison of theoretical predictions and experimental measurements, for different electric parameters. Figs. 5, 6 and 7 presents a detailed theoretical analysis of the pH-buffer interaction near the electrodes and the genesis of pH fronts through species concentration variations. Finally, Fig. 8 presents an experimental analysis of the pulse interaction with the pH-buffer fluctuation near the cathode as well as theoretical predictions.

Fig. 2 presents a DSC intravital microscopy image showing anodic and cathodic pH fronts obtained through the application of

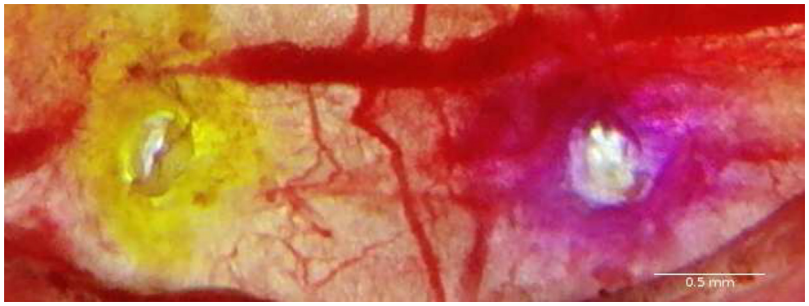

Fig. 2. 2D snapshot of pH fronts induced by GET (10 pulses of 40 V, 20 ms at 1Hz) in mice observed by intravital microscopy through a dorsal skinfold chamber. pH front visualization was done using phenol red ($C_{19}H_{14}O_5S$) as acid and basic indicator. Anodic acid front (left electrode) and cathodic basic front (right electrode) revealed as light yellow and pink-red areas, respectively. Thick and thin red stripes (hemoglobin) represent the capillary network. Image was taken 30 minutes after the end of the last pulse.

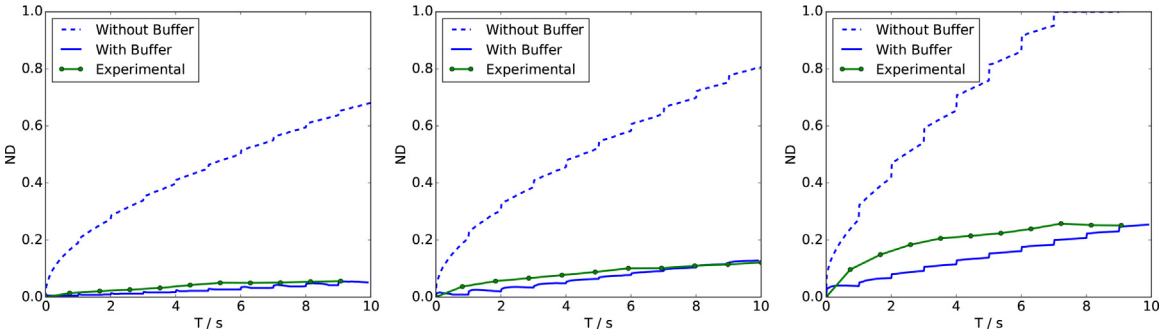

Fig. 3. Predicted (blue lines) and experimental (green lines) pH front tracking for a GET protocol with 10 pulses of 20 ms duration, at 1Hz and different electric fields: 20 V (left image), 40 V (center image) and 60 V (right image), respectively. Blue dashed and blue continuous lines indicate models without and with buffer, respectively. ND stands for the normalized sum of the distances covered by cathode and anode fronts (distance covered by the acid front from the anode plus distance covered by the basic front from the cathode divided by the anode-cathode separation: 2 mm).

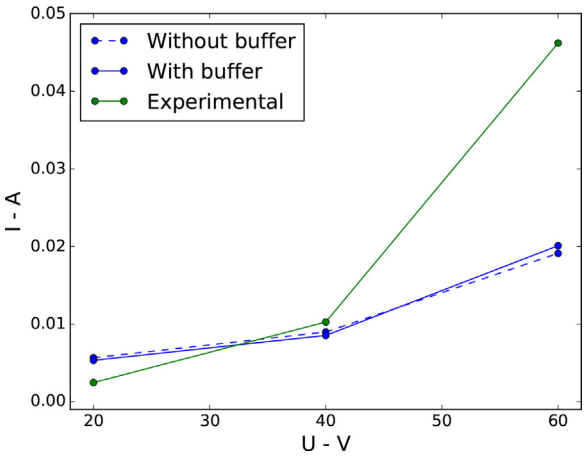

Fig. 4. Predicted (blue lines) and experimental (green line) electric current (I) vs applied applied voltage (U) for a GET protocol with 10 pulses of 20 ms duration, at 1Hz and different electric fields: 20 V, 40 V and 60 V. Blue dashed and blue continuous lines indicate models without and with buffer, respectively.

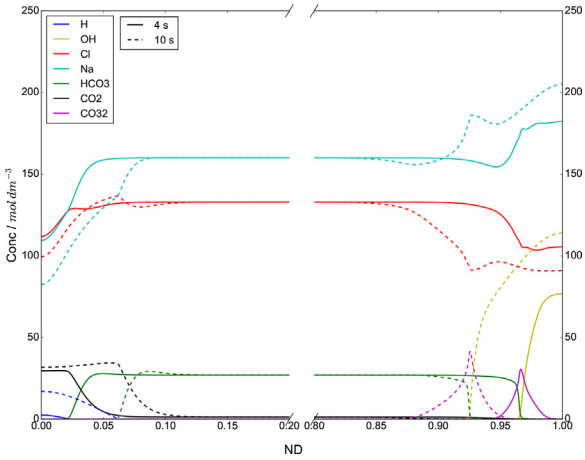

Fig. 7. Left pane: predicted ionic concentrations (hydrogen ions, bicarbonate, carbon dioxide, chloride and sodium) in a zone close to the anode (20% of the normalized anode-cathode distance) in a GET protocol (10 pulses of 20 ms at 1HZ with 40 V), at 4 s (continuous lines) and 10 s (dashed lines); right pane: the same, but considering CO_3^{2-} instead of CO_2 and OH^- instead of H^+, for a zone near the cathode (20% of the normalized anode-cathode distance).

a GET protocol (10 pulses of 20 ms at 1 Hz with 40 V) using a two needle electrode with a separation of 2 mm. The cathodic basic front (right electrode, pink-red area) and the anodic acid front (left electrode, light yellow area) are marked with phenol red. The image was taken 30 minutes after the end of the last pulse revealing the presence of pH fronts. It is remarkable not only their strength but also their extension in space and their persistence in time (of the order of minutes). This extended period of time for the physiological pH restoration is probably due to the presence of vascular lock, a well known and rather common phenomenon in GET protocols that reduces blood supply, thus blood-related natural buffering actions. These results suggest that pH fronts induce substantial damage near the electrodes. [19]

Before analyzing in detail the pH-buffer interaction it is worthwhile demonstrating the influence of including tissue buffer effects in the theoretical model of a GET protocol. For this goal, the space-time trajectory of a pH front will be used as a reliable variable synthesizing the complex chemical reactions taking place during the electrolysis process induced by the applied electric field. It will be assumed as damaged regions, the space-time regions covered by the pH=5.5 and 8.5 critical front trajectories, respectively. From now on, critical pH front trajectories will be referred as pH fronts. Prediction results will be presented for two different models: Sodium Chloride Model in which the tissue is treated as an aqueous solution of sodium chloride and the Buffering Model, in which the tissue is treated as an aqueous solution of sodium chloride plus the bicarbonate buffer system (bicarbonate (HCO_3^-), carbonate (CO_3^{2-}) and carbon dioxide (CO_2)). From now on, these models will be referred as models without and with buffer, respectively. Both are a 1D approximation, with the distance between electrodes being 2 mm and with the same effective diffusion coefficients. The model with buffer mimics GET experiments such as the one shown in Fig. 2; the model without buffer mimics an experimental GET gel model similar to that presented in [30].

Fig. 3 shows experimental and theoretical predictions of pH fronts for the models with and without buffer and for GET protocols with 10 pulses of 20 ms duration at a frequency of 1Hz and for different applied electric fields (20, 40 and 60 V). Results show that in the model with buffer (blue continuous line), pH fronts predictions and experimental measurements (green line) correlate quite well, though with a small departure for higher electric fields. In particular, pH fronts increase in time showing that they are partially neutralized by natural buffering. In the model without buffer (blue dashed line), pH fronts predictions and experimental measurements (green line) depart considerably. This departure is growing significantly in time due to the damping effect of natural tissue buffering, a departure that increases with

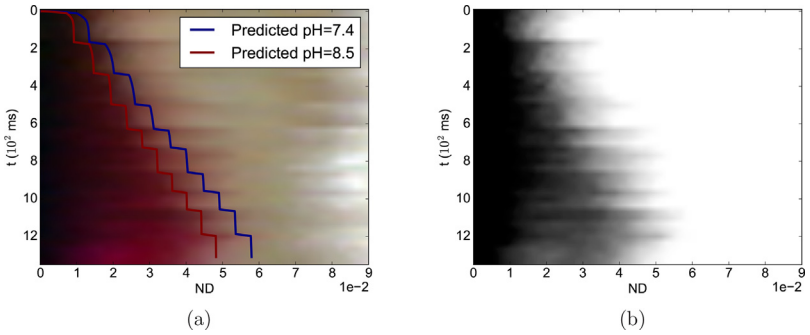

Fig. 8. a) Experimental space-time (ms) diagram of the evolution of the pulse interaction with the pH front-buffer fluctuation in a zone close to the cathode induced by a GET protocol (10 pulses of 10 ms at 10 Hz with 40 V) in mice observed by intravital microscopy through a dorsal skinfold chamber; red and blue lines are predicted pH=8.5 and 7.4 front trajectories. b) Gray scale threshold image of the left pane. ND stands for the normalized distance to the cathode.

higher electric fields. Since the same parameterization was used in both models, that is, they are similar except for the presence of the buffer, it is the damping effect of the buffering system that yields more realistic results. The immediate consequence of this is that buffer cannot be neglected in the simulations. The nature of the buffer damping effect on the pH front is explained below. It is worth mentioning that in our numerical modeling, conductivity is the same in the models with and without buffer; conductivity changes were included in the effective diffusion coefficient which was fitted with experimental measurements (establishing a compromise between measured electric current and pH fronts).

To further illustrate the influence of the tissue natural buffer in a GET protocol, Fig. 4 shows predicted electric current for the models with and without buffer (continuous and dashed blue lines, respectively) and for the experimental measurements (green line) vs. the applied voltage. A comparison of both theoretical models shows that the electric current is the same in both albeit the difference in pH fronts advance shown in the Fig. 3. This is because the electric current is distributed in a different way due to the different reactions taking place in each model. In the model with buffer, there is a decrease in mass transport due to the new reactions added. In the 20 V and 40 V cases, both models show a good correlation with experimental measurements. The lack of agreement of both models with experimental measurements for the 60 V case is probably due to the nonlinear behavior of ion mobility for higher fields that are not very well modeled through the effective diffusion coefficients.

A more detailed theoretical analysis of the evolution of the pH-buffer interaction close to the anode is presented next. Fig. 5(a) shows the predicted space-time evolution of hydrogen ion concentration corresponding to a GET protocol of 10 pulses of 20 ms at 1HZ with 40 V. The figure clearly shows the ON-OFF pulse behavior triggering the pH fluctuation. The pH = 5.5 yellow trajectory separates non-physiological from physiological pH values; the jagged shape also shows how pH front advance during the ON pulse and recedes during the OFF pulse. That is because, in the ON pulse, ion transport is mainly governed by migration and pH front shots forward; in the OFF pulse, ion transport is solely governed by diffusion and pH front recedes due to partial buffer neutralization. Moreover, the pH yellow trajectory increases in time until the last pulse, showing the accumulation of the pH variation. This demonstrates theoretically that the buffer is not able to neutralize the pH front during the GET protocol application (10 pulses). Fig. 5(b) presents a top view of the left image showing more clearly the evolution of the pH-buffer fluctuation.

To understand the genesis of pH fronts shown in Figs. 3 and 5, Fig. 6 left pane presents a snapshot at 980 ms after the last pulse of predicted main species concentrations from the models with and without buffer (H^+, OH^-, Cl^- and Na^+) or just with buffer (HCO_3^- and CO_2) in the anodic zone (GET protocol of 10 pulses of 20 ms

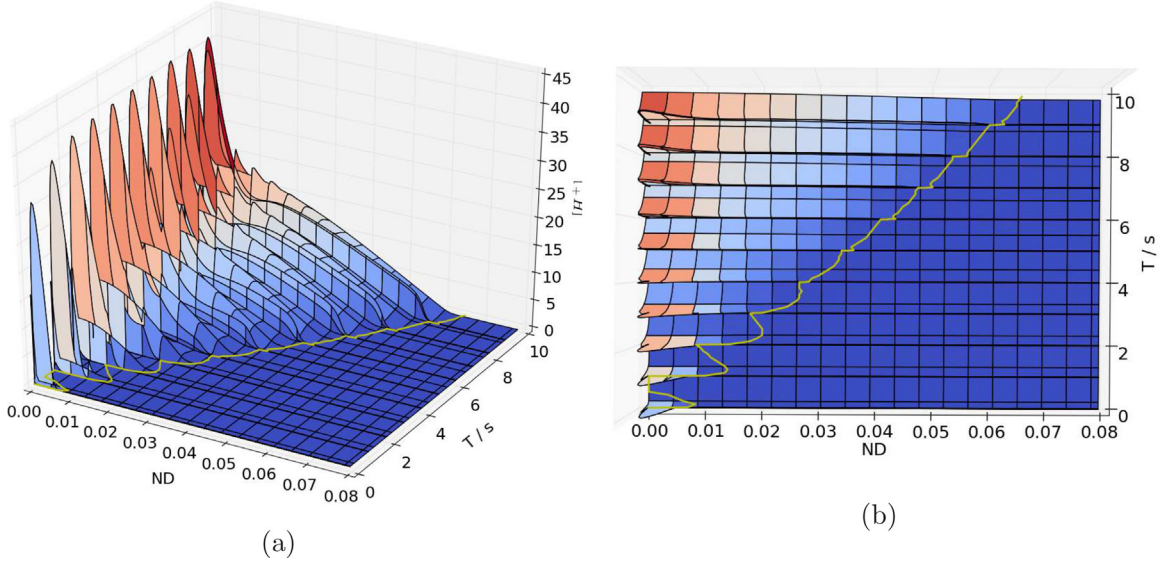

Fig. 5. a) Predicted space-time evolution of the hydrogen ion concentration in a GET protocol (10 pulses of 20 ms at 1HZ with 40 V). The pH=5.5 yellow trajectory separates non-physiological from physiological pH states, respectively. ND stands for the normalized distance to the anode. b) Top view of left image.

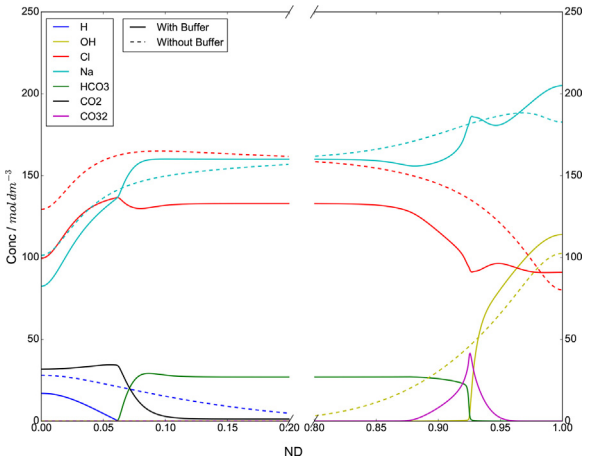

Fig. 6. Left pane: Predicted ionic concentrations (hydrogen ions, chloride and sodium) in a GET protocol (10 pulses of 20 ms at 1HZ with 40 V) in a zone close to the anode (20% of the normalized anode-cathode distance) in the model without buffer (dashed lines), and same species plus bicarbonate and carbon dioxide in the model with buffer (continuous lines); Right pane: same as left pane but considering CO_3^{2-} instead of CO_2 and OH^- instead of H^+, in the zone close to the cathode (20% of the normalized anode-cathode distance).

duration and frequency of 1 Hz at 40 V). Fig. 6 right pane shows the same but in the cathodic zone, considering CO_3^{2-} instead of CO_2 (CO_3^{2-} ion concentration is almost zero near the anode so it is not shown in the graph, the same for CO_2 near the cathode).

In Fig. 6 left pane, in the model with buffer, it is readily seen how the hydrogen front is limited by the bicarbonate presence, producing CO_2. In fact, in the buffer model (solid lines) at the place where protons and bicarbonate neutralize (close to ND=0.06), a maximum concentration of the products of reaction (4) occurs. Concomitantly, significant variations of sodium and chloride concentrations are observed, as compared to those appearing in the model without buffer (dashed lines). These variations are probably due to the electroneutrality condition imposed on the system.

Fig. 6 right pane shows, in the model with buffer, how the hydroxyl ion advance is hindered by its reaction with the bicarbonate ion, producing carbonate. Comparing models with and without buffer, the same tendency in the sodium and chloride curves is observed though the variations are much sharper (ND=0.93).

With the goal of analyzing the evolution in time of ion concentration in space in a GET protocol (10 pulses of 20 ms at 1 Hz with 40 V) in the model with buffer at different times, Fig. 7 left pane shows predicted ionic concentrations (hydrogen ions, bicarbonate, carbon dioxide, chloride and sodium) in a zone close to the anode, at 4 s (continuous lines) and 10 s (dashed lines). The snapshot at 4 s corresponds to an instant before the beginning of the fifth pulse (see Fig. 5(b)). The snapshot at 10 s corresponds to 980 ms after the last pulse. Fig. 7 right pane shows the same but considering CO_3^{2-} instead of CO_2 and OH^- instead of H^+, for a zone near the cathode (cathode is at the right and distances are measured relative to the anode).

At the anode (Fig. 7 left pane), due to the oxygen reaction (see appendix in [24]), hydrogen ions (blue line) are produced and transported towards the cathode by migration and diffusion. This transport is limited by its reaction with bicarbonate. As time evolves, hydrogen ion concentration increases over the anode-cathode distance. The bicarbonate (green line) evolves through a neutralization reaction (4) and by transport due to migration and diffusion. Also, bicarbonate concentration decreases over the anode-cathode distance. Chlorides are consumed in the chlorine reaction (see appendix in [24]) in such a way that its concentration decreases near the anode, releasing Cl_2 as a gas that leaves the system. As time evolves, chloride concentration decreases over the anode-cathode distance. There its curvature increase relative to the previous time probably due to the electroneutrality condition imposed on the system. Sodium (light blue line) is in charge of maintaining electroneutrality, therefore its concentration decreases near the anode; here again, there is a curvature increase relative to the previous time similar to the one discussed above. Carbon dioxide (black line) evolves as a product of the hydrogen-bicarbonate reaction (4). Its concentration reaches a maximum over the acid zone near the anode and starts decreasing as bicarbonate concentration increases. A comparison of carbon dioxide concentrations at 4 and 10 s shows an increase over the anode-cathode distance.

At the cathode (Fig. 7 right pane), hydroxyl ions are produced due to the hydrogen evolution reaction (see appendix in [24]) and transported by migration and diffusion. Hydroxyl transport is counterbalanced by its reaction with bicarbonate (6) and carbonate dioxide (5). As time lengthens, hydroxyl ion concentration increases at the cathode. The chloride concentration decreases near the cathode by electron repulsion with negative charges. On the contrary, sodium cation (Na^+) is attracted by negative charges at the cathode and increases its concentration. The carbonate ion (violet line) is produced in the hydroxyl-bicarbonate reaction (6) and is transported by migration and diffusion towards the anode. Carbon dioxide is almost zero near the cathode due to its reaction with the hydroxyl ion (5) and it is not shown in the graph (the same for CO_3^{2-} near the cathode). At the place where OH- encounters the bicarbonate ion, CO_3^{2-} shows a maximum.

An experimental analysis of the pulse interaction with the pH-buffer fluctuation is presented next. For this end, a GET protocol of 10 pulses of 10 ms at 10 Hz with 40 V, similar to the one used in Fig. 2, is applied. The time evolution of the pulse interaction with the pH-buffer fluctuation in a zone close to the cathode during the GET protocol is unveiled by the space-time diagram shown in Fig. 8 (left). Its construction was discussed in the in vivo modeling section. Here, each pixel line (equivalent to 6 μ) in the figure (dark-pink and light pink striped areas) corresponds to a time span of 33 ms. As previously discussed, the pixel lines are stacked to yield the space-time image spanning the duration of the experiment. The recording time starts at the first pulse and ends 152 ms after the last pulse, at a time beyond which migration has already ceased and pH fronts started a gradual decrease in time due to the buffer action. In spite of this action, pH fronts remain covering a region of space close to the electrodes for several minutes (as seen, for instance, in Fig. 2). The synchronization between the electric pulses and the pH-buffer fluctuation was done in the following way: the experiment was recorded continuously at 30 frames per second, the exact frame at which a pulse was triggered was chosen as the frame at which an abrupt change of pH dye occurred. Fig. 8 (left) shows a period of time from the first pulse triggered at time 0 until 152 ms after the tenth pulse (triggered at 1188 ms). In our experiments, the BTX ECM 830 pulse frequency was not uniform, for instance, the first four pulses started at 0, 165, 330 and 495 ms, respectively. This non-uniform pulse frequency behavior is reflected in the non-uniform distribution of the pH-buffer fluctuation as clearly observed in Fig. 8. Approximately, 41 lines are seen in the figure, roughly totaling 1350 ms, the time span of the recording. These results show experimentally how the basic pH front (pink area) jump forward during the ON pulse and move backward during the OFF pulse. There is a close correspondence between the ON-OFF pulse cycle and pH front fluctuation, the pulse length and frequency tuning the pH-buffer behavior. It is worth

remarking that the tissue natural buffer is not able to completely neutralize the pH front during the OFF pulse, as shown by the steady increase of the pink area in time. This suggests that regions enclosed by pH fronts and close to the electrodes may be substantially damaged since they have been during sufficient time at very high pH values.

For comparison purposes, in Fig. 8, predicted pH=8.5 and 7.4 critical pH front trajectories (red and blue lines) are superimposed over the experimental ones. Red and blue lines trajectories shot forward and move backward during the electric ON-OFF pulse cycle. The net expansion in time of these trajectories, as shown in the figure, demonstrates theoretically that the bicarbonate buffer is not able to neutralize the pH front. It is remarked that migration is a much stronger ion transport mode than diffusion, and prevails, even that its action time is more than three times smaller than that of diffusion. The figure shows an excellent correlation between pulse and pH fronts fluctuation, the pulse frequency and length tuning the pH-buffer behavior. There is also an excellent correlation between predicted and experimental pH front trajectories. Fig. 8 (right) presents a gray scale image of the left pane showing more vividly the pH-buffer fluctuation and how the pH starts decreasing after the last pulse.

It is interesting to recall the electrochemical analogy between GET, a protocol in which damage must be minimized, and EA, a protocol whose aim is to induce damage. As shown in [31,24], damage in an EA protocol is proportional to the Coulomb dosage (the electric current multiplied by the time of its application) pumped into the tissue; this is measured by the region of tissue covered by a rather smooth pH trajectory (as illustrated in [32], figure 3). By the same token, in a GET protocol, the damage is proportional to the Coulomb dosage (where Coulomb dosage is the product of the electric current multiplied by the number of pulses and by pulse length) and is measured by the region of tissue covered by a jagged pH front trajectory (as seen in Fig. 8). In a GET protocol Coulomb dosage is much smaller than in an EA; though damage is also smaller, still may be considerable. Since damage is a function of the Coulomb dosage, the possibility opens for optimizing GET protocols by diminishing damage through an appropriate choice of the electric current, pulse number, and pulse length.

In summary, the products of electrolysis reactions at the electrodes, in particular, pH fronts, unavoidably generate acid and basic pH fronts. While away from the electrodes these fronts are normally balanced by the tissue natural buffer; near the electrodes, this balance is broken and substantial damage may occur. For instance, in our in vivo experiments, with an electrodes separation of 2 mm, the pH front advancement was 0.5 mm, that is, 25 % of the distance between electrodes. Considering that the line between electrodes is 100 % electroporated, it is safe to assume that 25 % of it is damaged. One way to minimize damage could be to decrease pulse length compensating with pulse amplitude and pulse number. Particularly, the contribution of pulse length to damage seems to be more important. This procedure was shown to produce less intense pH changes in the tissue [18] consequently increasing GET efficiency as shown in [33].

4. Conclusion

Pre-clinical protocols based on plasmids delivered by GET are opening promising perspectives in many therapeutic fields, and in particular in cancer treatments. Many different factors influencing the efficiency of this new strategy should be considered and studied deeper. Among these, the presence of tissue natural buffering has not yet been considered in theoretical modeling. Here, we introduced an in-silico GET model assuming a tissue with a bicarbonate buffer system, thus allowing the analysis of pH fronts-natural buffering interaction. The model is validated with intravital microscopy measurements in a dorsal skinfold chamber in a mouse model. The in-silico model uses the Nernst-Planck equation for ion transport in a seven-component electrolyte (H^+, OH^-, Cl^-, Na^+, HCO_3^-, CO_2 and CO_3^{2-}), electroneutrality conditions and Butler-Volmer equations.

Experimental measurements and theoretical predictions show a close correlation between electric pulses and pH fronts-buffer interaction: during the ON pulse pH jumps forward, during the OFF cycle, pH fronts move backward due to tissue natural buffer neutralization. However, this neutralization is not sufficient to compensate pH front advancement, the net result being pH front increase in time. Moreover, experiments show and theory confirms that regardless of the presence of tissue natural buffer attenuation, pH fronts remain during several minutes in a non-physiological state after the treatment. In brief, the products of electrolysis reactions at the electrodes, in particular pH fronts, unavoidably generate acid and basic pH fronts. While away from the electrodes these fronts are normally balanced by the tissue natural buffer; near the electrodes this balance is broken and substantial damage may occur. Ways for minimizing GET damage suggests pulse shortening and voltage rise for compensation.

Acknowledgements

M. Marino and F. Maglietti have a scholarship from the Consejo Nacional de Investigaciones Científicas y Técnicas (CONICET) Argentina; N. Olaiz, G. Marshall, and S. Michinski are researchers at CONICET; E. Signori is a researcher at CNR-Rome, Italy. This work was supported by grants from CONICET PIP 379/12, Universidad de Buenos Aires UBACyT 2014/17 and the International European Cooperation in Science and Technology (COST Action TD 1104). E. Signori was partially supported by CNR-Short Term Mobility fellowship 2016. The founders had no role in the study, design, data collection, analysis, decision to publish, or preparation of the manuscript.

References

[1] D. Miklavčič, Network for Development of Electroporation-Based Technologies and Treatments: COST TD1104, The Journal of Membrane Biology 245 (10) (2012) 591–598, doi:http://dx.doi.org/10.1007/s00232-012-9493-8.
[2] R. Cadossi, M. Ronchetti, M. Cadossi, Locally enhanced chemotherapy by electroporation: clinical experiences and perspective of use of electrochemotherapy, Future Oncology 10 (5) (2014) 877–890.
[3] C. Jiang, R.V. Davalos, J.C. Bischof, A review of basic to clinical studies of irreversible electroporation therapy, IEEE Transactions on Biomedical Engineering 62 (1) (2015) 4–20, doi:http://dx.doi.org/10.1109/TBME.2014.2367543.
[4] L.M. Mir, Nucleic acids electrotransfer-based gene therapy (electrogenetherapy): Past current and future, Molecular Biotechnology 43 (2) (2009) 167–176, doi:http://dx.doi.org/10.1007/s12033-009-9192-6.
[5] B. Kos, P. Voigt, D. Miklavcic, M. Moche, Careful treatment planning enables safe ablation of liver tumors adjacent to major blood vessels by percutaneous irreversible electroporation (IRE), Radiology and Oncology 49 (3) (2015) 234–241, doi:http://dx.doi.org/10.1515/raon-2015-0031.
[6] M. Tschon, F. Salamanna, M. Ronchetti, F. Cavani, A. Gasbarrini, S. Boriani, M. Fini, Feasibility of Electroporation in Bone and in the Surrounding Clinically Relevant Structures: A Preclinical Investigation, Technol Cancer Res Treat (1533-0338 (Electronic)). doi:10.1177/1533034615604454.
[7] E. Neumann, M. Schaefer-Ridder, Y. Wang, P.H. Hofschneider, Gene transfer into mouse glioma cells by electroporation in high electric fields, EMBO J. 1 (7) (1982) 841–845, doi:http://dx.doi.org/10.1385/1-59259-409-3:55.
[8] Marino M, Olaiz N, Signori E, Maglietti F, Suarez C, Colombo L, Turjanski P, Michinski S, Luján E, Marshall G. (2014). Tissue damage in vaccination protocols based on electroporation: pH fronts and tissue natural buffering. Book of Proceedings from 14th International Conference on Progress In Vaccination against Cancer PIVAC-14, 24-26-September 2014, Rome, Italy, abstract 22, page 43. Poster available from: https://www.researchgate.net/profile/Nahuel_Olaiz/publication/266317861.
[9] T.K. Wong, E. Neumann, Electric field mediated gene transfer, Biochemical and biophysical research communications 107 (2) (1982) 584–587.
[10] P. Chiarella, V.M. Fazio, E. Signori, Electroporation in DNA vaccination protocols against cancer, Current drug metabolism 14 (3) (2013) 291–299.

[11] J.-M. Escoffre, T. Portet, L. Wasungu, J. Teissie, D. Dean, M.-P. Rols, What is (Still not) Known of the Mechanism by Which Electroporation Mediates Gene Transfer and Expression in Cells and Tissues, Molecular Biotechnology 41 (3) (2009) 286–295, doi:http://dx.doi.org/10.1007/s12033-008-9121-0.
[12] C. Rosazza, S.H. Meglic, A. Zumbusch, M.-P. Rols, D. Miklavcic, Gene Electrotransfer: A Mechanistic Perspective, Current gene therapy 16 (2) (2016) 98–129, doi:http://dx.doi.org/10.2174/1566523216666160331130040.
[13] E. Nilsson, H. von Euler, J. Berendson, A. Thörne, P. Wersäll, I. Näslund, A. Lagerstedt, K. Narfström, J. Olsson, Electrochemical treatment of tumours, Bioelectrochemistry 51 (2000) 1–11.
[14] M. Phillips, N. Raju, L. Rubinsky, B. Rubinsky, Modulating electrolytic tissue ablation with reversible electroporation pulses, TECHNOLOGY 3 (1) (2015) 1–9, doi:http://dx.doi.org/10.1142/S233954781550003X.
[15] D. Lando, S. Haroutiunian, A. Kul'ba, E. Dalian, P. Orioli, S. Mangani, A. Akhrem, Theoretical and experimental study of DNA helix-coil transition in acidic and alkaline medium, J Biomol Struct Dyn 12 (2) (1994) 355–366.
[16] R. Dubey, D. Tripathi, A study of thermal denaturation/renaturation in DNA using laser light scattering: a new approach, Indian Journal of Biochemistry & Biophysics 42 (2005) 301–307.
[17] H. von Euler, E. Nilsson, J. Olsson, A. Lagerstedt, Electrochemical treatment (EChT) effects in rat mammary and liver tissue. In vivo optimizing of a dose-planning model for EChT of tumours, Bioelectrochemistry 54 (2001) 117–124.
[18] F. Maglietti, S. Michinski, N. Olaiz, M. Castro, C. Suárez, G. Marshall, The role of Ph fronts in tissue electroporation based treatments, PLoS ONE 8 (11) (2013) 1–8, doi:http://dx.doi.org/10.1371/journal.pone.0080167.
[19] N. Olaiz, E. Signori, F. Maglietti, a. Soba, C. Suárez, P. Turjanski, S. Michinski, G. Marshall, Tissue damage modeling in gene electrotransfer: The role of pH, Bioelectrochemistry 100 (October 2015) (2014) 105–111, doi:http://dx.doi.org/10.1016/j.bioelechem.2014.05.001.
[20] E. Nilsson, J. Berendson, E. Fontes, Electrochemical treatment of tumours: a simplified mathematical model, J Electroanal Chem 460 (1-2) (1999) 88–99, doi:http://dx.doi.org/10.1016/S0022-0728(98)00352-0.
[21] E. Nilsson, J. Berendson, E. Fontes, Development of a dosage method for electrochemical treatment of tumours: a simplified mathematical model, Bioelectrochem Bioenerg 47 (1998) 11–18.
[22] E. Nilsson, E. Fontes, Mathematical modelling of physicochemical reactions and transport processes occurring around a platinum cathode during the electrochemical treatment of tumours, Bioelectrochemisty 53 (2) (2001) 213–224, doi:http://dx.doi.org/10.1016/S0302-4598(01)00097-6.
[23] P. Turjanski, N. Olaiz, P. Abou-Adal, C. Suárez, M. Risk, G. Marshall, pH front tracking in the electrochemical treatment (EChT) of tumors: Experiments and simulations, Electrochimica Acta 54 (26) (2009) 6199–6206, doi:http://dx.doi.org/10.1016/j.electacta.2009.05.062.
[24] E. Luján, H. Schinca, N. Olaiz, S. Urquiza, F.V. Molina, P. Turjanski, G. Marshall, Optimal dose-response relationship in electrolytic ablation of tumors with a one-probe-two-electrode device, Electrochimica Acta 186 (October) (2015) 494–503, doi:http://dx.doi.org/10.1016/j.electacta.2015.10.147.
[25] J. Newman, K. Thomas-Alyea, Electrochemical Systems, 3rd Edition, John Wiley & Sons, Inc, Hoboken, New Jersey, 2004.
[26] J.M. Grime, M.A. Edwards, N.C. Rudd, P.R. Unwin, Quantitative visualization of passive transport across bilayer lipid membranes, PNAS 105 (38) (2008) 14277–14282.
[27] O. Siggaard-Andersen, The Acid-Base Status of the Blood, 4th Edition, Munksgaard, 1974.
[28] A. Arieff, Fluid, electrolyte, and acid-base disorders, 2nd Edition, Churchill Livingstone, New York, 1995.
[29] G. Marshall, Solución Numérica de Ecuaciones Diferenciales. Tomo II: Ecuaciones en Derivadas Parciales, Editorial Reverté S.A., Buenos Aires, 1986.
[30] P. Turjanski, N. Olaiz, F. Maglietti, S. Michinski, G. Marshall, C. Suárez, F.V. Molina, G. Marshall, C. Suárez, F.V. Molina, G. Marshall, The role of pH fronts in reversible electroporation, PLoS ONE 6 (4) (2011) e17303, doi:http://dx.doi.org/10.1371/journal.pone.0017303.
[31] G. Marshall, Mass Transfer of Electrolytic Species During Electric Field-Based Tumor Treatments, Springer International Publishing, Cham, 2016, pp. 1–18, doi:http://dx.doi.org/10.1007/978-3-319-26779-1_68-1. URL https://doi.org/10.1007/978-3-319-26779-1_68-1.
[32] N. Olaiz, F. Maglietti, C. Suárez, F.V. Molina, D. Miklavcic, L. Mir, G. Marshall, D. Miklavcicc, L. Mir, G. Marshall, Electrochemical treatment of tumors using a one-probe two-electrode device, Electrochimica Acta 55 (20) (2010) 6010–6014, doi:http://dx.doi.org/10.1016/j.electacta.2010.05.057.
[33] R. Heller, C.M. Lundberg, N. Burcus, C. Edelblute, S. Guo, Gene electrotransfer of plasmids encoding cytokines as an effective immunotherapy approach for melanoma, The Journal of Immunology 196 (1 Supplement) (2016) 213–216.
[34] D.R. Lide, CRC Handbook of chemistry and physics, 80th Edition, CRC Press, 1999.
[35] A. Tamimi, E.B. Rinker, O.C. Sandall, Diffusion coefficients for hydrogen sulfide carbon dioxide and nitrous oxide in water over the temperature range 293-368 K, Journal of chemical and engineering data 39 (2) (1994) 330–332.
[36] J.B. West, Physiological Basis of Medical Practice, 11th Edition, Lippincott William & Wilkins, Baltimore, USA, 1985.
[37] W.J. Moore, Basic Physical Chemistry, Prentice-Hall Int Ed, London, 1983.